ELSEVIER

Contents lists available at ScienceDirect

Atmospheric Research

journal homepage: www.elsevier.com/locate/atmosres



Identification and forecasting of low-level wind shear based on long range Doppler wind lidar

Anning Chen^a, Jinlong Yuan^{a,*}, Haoyu Yang^a, Jiaxiu Liu^a, Yuanhao Gu^a, Yue Liu^a, Tianwen Wei^a, Haiyun Xia^{a,b}

ARTICLE INFO

Keywords: Wind shear Shear line Coherent Doppler wind lidar Cluster analysis

ABSTRACT

Low-level wind shear poses a threat to the safety of aircraft during take-off and landing, while its precise detection remaining a critical challenge in meteorological monitoring. To solve this problem, this study proposes a method for the identification of low-level wind shear and shear line based on coherent Doppler wind lidar. The method integrates a ramp detecting algorithm and a dual filtering mechanism for wind shear identification, subsequently applying spatial clustering analysis to reconstruct low-altitude wind shear lines. An airport field experiment demonstrates effective detection of shear lines induced by gust fronts and convective weather systems. An urban field campaign verifies the practicality in detecting shear lines of complex underlying surface, achieving a maximum forecast of approximately 25 min through spatial distribution and wind field analysis. This study provides technical support to improve the extreme weather warning capability and ensure the safety of low-altitude flights.

1. Introduction

Wind shear is defined as a sudden and significant change in wind speed or direction, typically manifesting as vertical or horizontal gradients (ICAO, 2005). A shear line is a narrow and long region of concentrated wind field discontinuities, with pronounced velocity or directional gradients. Wind shear frequently co-occurs with thunderstorms and frontal systems, posing significant risks to civil aviation and low-altitude operations (Luers and Hairies, 1983; Nechaj et al., 2019). Therefore, effective wind shear detection is critical for ensuring personnel safety, mitigating property losses, and optimizing flight efficiency. Particularly the rapid expansion of China's low-altitude aviation economy necessitates the development of high-precision low-level wind shear warning systems (Huang, 2025).

Common atmospheric wind field detection equipment includes surface anemometers, Doppler weather radar, and Doppler wind lidar, etc. However, surface anemometers exhibit constrained vertical detection range due to single-point sampling limitations. Doppler weather radar effectively detects large particles in precipitation environments (Wadler et al., 2023; Wilson et al., 1984), whereas lidar achieves clear-air low-level wind shear identification (Huang et al., 2024; Liu et al., 2019;

Shear line identification, as an important component of meteorological monitoring, has gone through an evolutionary process from manual analysis to intelligent recognition. The initial phase relied on artificial weather map analysis, with empirical adaptations and subjective limitations. Numerical wind field analysis methods achieve identification by quantifying gradient parameters (e.g. wind direction, vorticity), but exhibit missing detection in complex wind fields with multi-scale coupling (Bluestein and Speheger, 1995; Piva et al., 2008).

E-mail address: yuanjinlong@nuist.edu.cn (J. Yuan).

^a School of Atmospheric Physics, Nanjing University of Information Science & Technology, Nanjing 210044, China

^b School of Earth and Space Science, University of Science and Technology of China, Hefei 230026, China

Thobois et al., 2018; Zhang et al., 2019; Zhao et al., 2025). Lidar can provide more accurate detection data even under complex surface conditions (Luo et al., 2024; Yang et al., 2024), owing to its high spatial and temporal resolution (Su et al., 2024; Wang et al., 2021; Wang et al., 2024). Current warning algorithms comprise ramp detecting algorithm (Chan and Shun, 2008), F-factor algorithm (Chan, 2012; Chan et al., 2011; Lee and Chan, 2013), eddy dissipation rate algorithm (Hon and Chan, 2014) and hybrid approaches (Zhao et al., 2025), etc. F-factor or eddy dissipation rate algorithm focuses on quantifying the severity of shear by defining the single metric to identify wind shear, with limitations on scene adaptability. Their research primarily focuses on wind shear monitoring in glide path areas, while studies on full-region detection remain limited, particularly in shear line identification.

^{*} Corresponding author.

Doppler weather radar implementation enhanced mesoscale feature detection (e.g., convergence lines, gust fronts) within precipitation systems (Hermes et al., 1993; Huang et al., 2019; Tian et al., 2024), while beam attenuation effect and signal obstruction constrain low-altitude weak shear identification. In recent years, machine learning algorithms have demonstrated considerable potential in addressing complex nonlinear relationships, emerging as new approach for shear line identification (Biard and Kunkel, 2019; Cai et al., 2021; Lagerquist et al., 2019; Liu et al., 2022; Tian et al., 2024). However, issues such as poor interpretability and high dependence on the datasets cannot be ignored. Consequently, developing more efficient and reliable algorithms for low-altitude smaller scale shear line detection remains challenging.

In view of the challenges of low-altitude wind shear detection in complex environments, this study proposes a method for the identification of low-level wind shear and shear line based on coherent Doppler wind lidar. It is organized as follows: theoretical basis of the method is introduced in Section 2. The effectiveness of the method in airport experiment and urban complex surface shear identification is verified in Section 3. Finally, discussion and conclusion are drawn in Section 4.

2. Methodology

This study proposes a novel wind shear and shear line identification method that integrates ramp detecting algorithm and a dual filtering mechanism. Unlike previous algorithms it involves the processing of all radial wind speed from Plan Position Indicator (PPI) scanning, which could ensure full-region wind shear detection as basis of shear line reconstruction. Wind shear identification is subject to interference from irrelevant scale variations, such as short-range with high-gradient and long-range ones with weak gradients. Therefore, scales filtering is particularly important in the identification process. A dual screening mechanism is set to eliminate these interferences and ensure precise identification of significant wind shear ramps (distance segments with speed changes). The dual filtering mechanism includes wind shear intensity factor (Chan and Shun, 2008; Zhao and Shan, 2022) and total wind shear value (WSV) factor to effectively identify wind shear ramps above thresholds. The wind shear intensity factor is derived from the Sfactor, which first proposed by Woodfield and Woods, 1983 (Woodfield and Woods, 1983). S factor is defined as follows:

$$S = \left(\frac{dV}{dt}\right)g\left(\frac{\Delta V}{V_a}\right)^2 = \left(\frac{\Delta V}{(\Delta L)^{1/3}}\right)^3 gV_a^{-1} \tag{1}$$

where dV/dt represents the change rate of wind speed; ΔV represents the variation of wind speed; V_a represents the aircraft's approach speed when landing, which is usually constant; and ΔL represents the ramp length corresponding to ΔV . This factor measures the strength of wind shear, the magnitude of which depends largely on the $\Delta V/(\Delta L)^{1/3}$. Therefore, the S factor simplifies to $\Delta V/(\Delta L)^{1/3}$ in detecting wind shear. The proposed method also achieves the identification of regional shear lines by extracting the shear points of ramps for cluster analysis and filtering the clusters that meet the conditions for curve fitting. Fig. 1 illustrates the flowchart of the proposed methodology, which comprises the following key steps:

Step 1. Extraction of wind shear ramps from radial wind speed. Radial wind speed is retrieved from the lidar spectrum. The invalid and isolated data points are eliminated through quality control. The radially wind speed from the raw inversion contains noise, which tends to overestimate small changes on small scales causing false wind shear identification. Processing with smoothing formula can reduce random errors. The smoothing formula is defined in Eq. (2).

$$U_1(i) = \frac{1}{4}U_0(i-1) + \frac{1}{2}U_0(i) + \frac{1}{4}U_0(i+1), (i=1,2,3,...,N)$$
 (2)

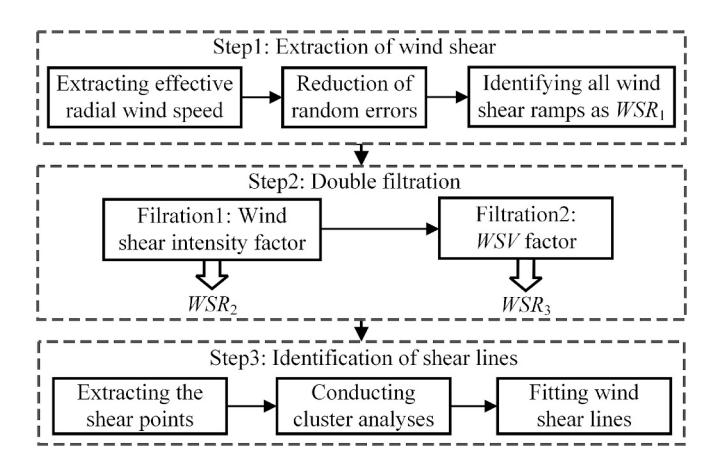


Fig. 1. Flowchart of the method for identifying wind shear and shear line. It includes three steps: extraction of wind shear, double filtration, and identification of shear lines.

where U_1 is the wind speed after smoothing, U_0 is the original wind speed, i represents the data point serial number, and N represents the total number of valid data point. All potential ramps are comprehensively detected by varying the wind shear ramp detection length (Yuan et al., 2022), to obtain wind shear ramps collection of WSR_1 .

Step 2. Double filtering strong wind shear ramps. Wind shear ramps WSR_2 are initially filtered out from the WSR_1 , when the wind shear intensity factor $\Delta V/(\Delta L)^{1/3}$ exceeding the preset threshold. Subsequently, the WSV value of each wind shear ramp in the WSR_2 is calculated (Baranov and Lemishchenko, 2020). Then strong wind shear ramps WSR_3 are further filtered by comparing with the preset WSV criteria. The WSV value for a single wind shear ramp is calculated as follows.

The mean velocity of the wind shear ramp is calculated based on the corresponding wind speed and position of the velocity nodes within the ramp as well as the length of the ramp. The mean velocity \overline{V} is calculated by

$$\overline{V} = \frac{1}{2} \frac{\sum_{j=1}^{J-1} (V_j + V_{j+1}) (l_{j+1} - l_j)}{\Delta L}$$
(3)

where J denotes the total number of velocity nodes in the wind shear ramp, j denotes velocity node serial number, V and l denote the wind speed and position of corresponding node, respectively. And the total value of the wind energy S_0 is calculated by:

$$S_0 = \frac{1}{2} \sum_{j=1}^{J-1} (V_j^2 + V_{j+1}^2) (l_{j+1} - l_j)$$
(4)

Under the continuous approximation, the total value of wind energy can be expressed as:

$$S_0 = \int_{-\frac{\Delta L}{2}}^{\frac{\Delta L}{2}} (\overline{V} + \alpha x)^2 dx \tag{5}$$

where α measures the change in wind speed per unit distance and x represents the position of the measuring point relative to the center of the ramp. The integral result is:

$$S_0 = \overline{V}^2 \Delta L + \alpha^2 \frac{\Delta L^3}{12} \tag{6}$$

Then, the expression for α can be derived as:

$$\alpha = \sqrt{\frac{12}{\Delta L^2} \left| \frac{S_0}{\Delta L} - \overline{V}^2 \right|} \tag{7}$$

where the sign of the α factor is determined by the tendency of the wind shear ramp to increase or decrease in velocity. The α factor takes into

account the wind shear accumulated by the wind speed jitter in the ramp, which distinguishes it from the traditional ramp detecting algorithm (which takes into account the wind shear at both ends or linear fitting). Using this factor can identify the wind shear more accurately and filter the eligible wind shear ramps. Finally, the total wind shear value of the ramp is calculated by:

$$WSV = \sqrt{\frac{2}{3}} \cdot \alpha \cdot \Delta L \tag{8}$$

It is worth stating that different aircrafts have different sensitivities to wind shear. Civil airplanes are more sensitive to strong shear, whereas smaller aircrafts with low speeds such as unmanned aerial vehicles (UAVs) can lose their balance even weak wind shear. Consequently, the threshold and criteria should be dynamically adjusted based on regional wind field characteristics and shear intensity to meet the monitoring needs of different aircraft. Shear characteristics and intensity vary across different weather, setting different thresholds is essential for enhancing the accuracy of identification. For regions with higher wind speeds and stronger shear, a higher threshold could focus on significant shear, thus improving detection efficiency. On the contrary, for scenarios with weaker wind fields and less intense shear, the threshold is lowered to improve the detection sensitivity of relatively weak but meaningful shear. Fig. 2 demonstrates a typical identification result of a single radial wind shear in the strong convective weather. The blue shading regions in Fig. 2a represent detected strong wind shear ramps, while Fig. 2b quantifies the shear intensity for each identified ramp with WSV factor. Considering that range resolution of lidar is 30–150 m (Xia et al., 2024), the initial ramp detection length is set to 300 m in this case. Due to the high wind speeds and strong wind shear caused by strong convective weather, the wind shear intensity factor $\Delta V/(\Delta L)^{1/3}$ threshold is set to 0.5 based on a series of data validation, which can effectively focus on the strong wind shear. The three ramps with the maximum WSV are selectively extracted. A pronounced strong wind shear zone is observed between the distance of 5.9-8.6 km, characterized by maximum speed difference exceeding 16.0 m s⁻¹ and the WSV value reaching -14.9 m s^{-1} .

Step 3. Identification of shear lines. Steps 1 and 2 are iteratively applied to all azimuthal radial velocity, thereby extracting all strong wind shear ramps WSR_{total} across the scanning area. Then the location of the shear points is recorded for each wind shear ramp in the WSR_{total} . Specifically, if a wind shear ramp appears a sudden directional change, the inflection point of this discontinuity is designated as the shear point. For ramps with homogeneous wind direction, the center point of the ramp is assigned as the shear point.

Most of the shear points in the area show significant linear distribution characteristics, accompanied by a small number of randomly

dispersed noise points. This distribution suggests that by connecting these linearly distributed shear points, a continuous shear line can be constructed. It could extend the detection scope from local radial shear to regional wind shear identification. However, these non-negligible dispersed noise points may interfere with the precise determination of the shear line position. Therefore, shear points clustering analysis is performed to aggregate spatially adjacent valid shear points while filtering out the isolated noise points. The position coordinate of the shear point (r_k, θ_k) is converted to Cartesian coordinates (x_k, y_k) , where r_k represents the lidar-to-point distance, θ_k represents the azimuth angle, and k is the serial number of the shear point. An initial shear point is randomly selected as the cluster center, around which a circular region with radius R_{min} (minimum distance threshold) is defined. Unclassified shear points within this region are merged into the cluster, and continue searching around each new point while excluding classified ones until all points are clustered. After clustering analysis, the resulting clusters include not only the linear feature clusters but also invalid clusters. Firstly, a threshold for the minimum number of shear points in cluster is set to exclude small clusters. Then, the estimated curve length of each cluster is calculated using distance formula. Only clusters with lengths exceeding a preset threshold are selected for curve fitting, effectively filtering out compact point groups. Finally, qualifying clusters undergo curve fitting to reconstruct shear lines across the scanning area. Fig. 3a-c show the typical results of shear points identification and clustering at different moments in the scanning area. In the case, the minimum distance R_{min} is defined as 1 km, and the threshold of total number of shear points in the cluster is set to 8. The black dots denote the points that do not satisfy the clustering conditions, while the other dots of different colors denote the different clusters of shear points.

3. Experiments and results

3.1. Shear identification experiment of airport field

The wind shear detection experiment was previously conducted at Kunming Changshui International Airport, China (Xia et al., 2024), where a long range lidar with 30 km was applied. To validate the applicability of the method, two distinct weather events are analyzed: a severe convective process and a gust front process. If not specified, local time is used.

At 17:38 on March 18, 2022, the flight OTC7157 reported encountering wind shear of undetermined intensity, during the take-off stage. Fig. 4 shows the wind shear identification results at 3° elevation angle and 333° azimuth at different times. At 17:01, significant wind shear was observed during 6.1–10.1 km with a wind speed difference of 17.8 m s⁻¹, with the *WSV* value of -11.7 m s⁻¹. Subsequently at 17:23, four

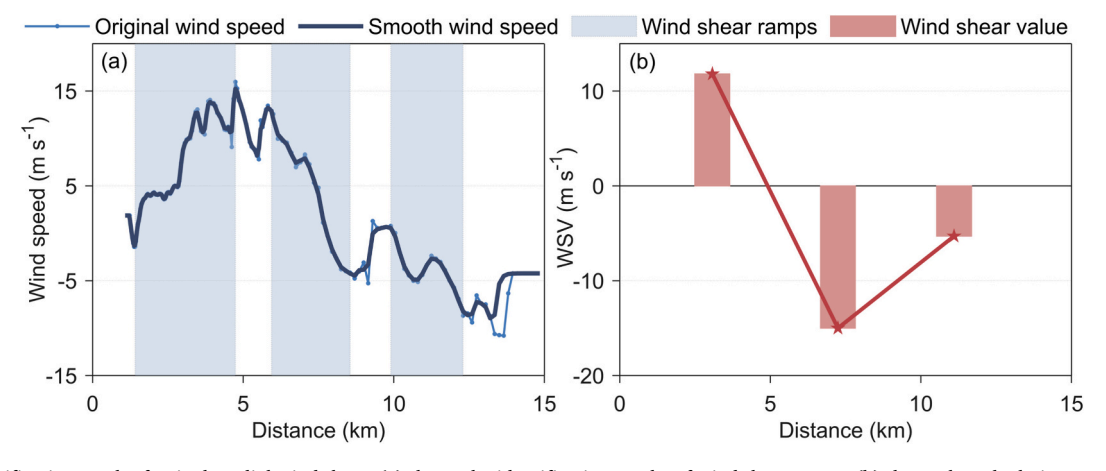


Fig. 2. The identification result of a single radial wind shear. (a) shows the identification results of wind shear ramps. (b) shows the calculation results of the WSV of the ramps.

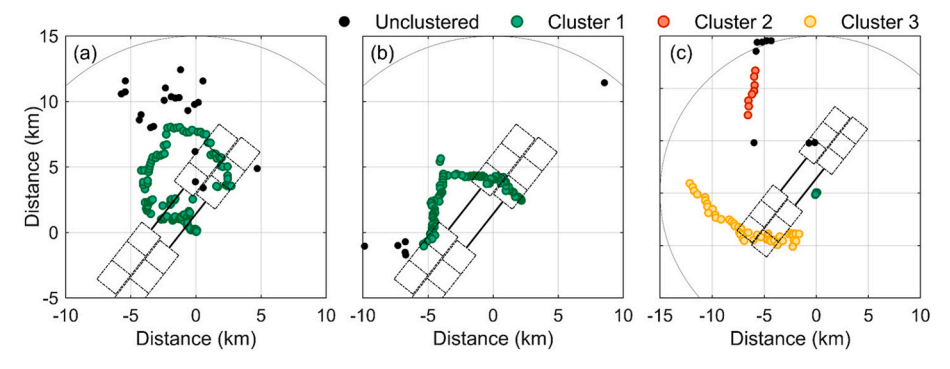


Fig. 3. Results of typical clustering. (a)-(c) are the identification and clustering results of shear points at different moments in the scanning area. The black solid and dashed boxes represent the airport runway and glide path, respectively.

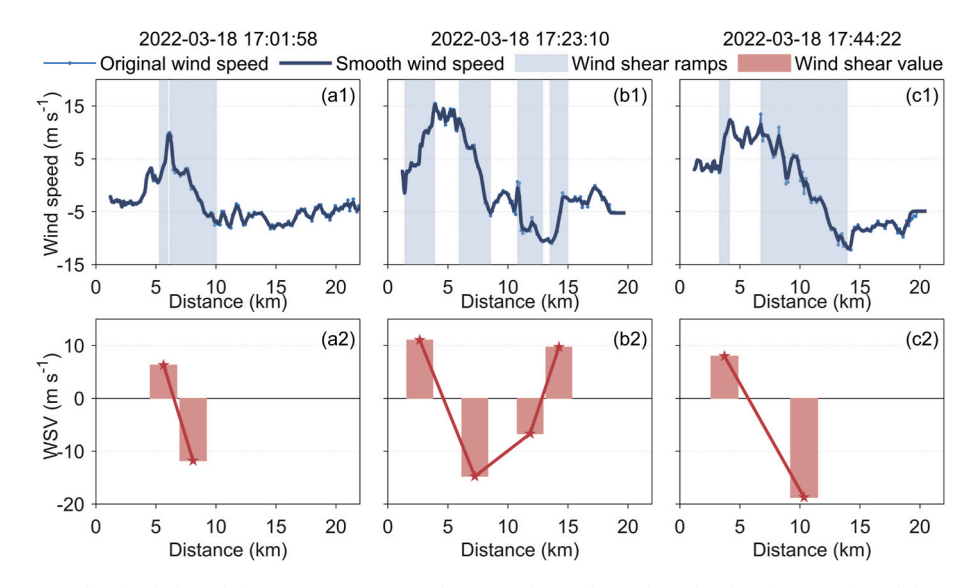


Fig. 4. Typical identification results of radial wind shear in convective weather. (a1), (b1) and (c1) show the identification of wind shear ramps at different times for 3° elevation angle and 333° azimuthal angle, respectively. (a2), (b2) and (c2) represent the *WSV* value of each wind shear ramp.

wind shear ramps were detected during the distance of 1.4–15.0 km. The speed difference of the strongest wind shear ramp reached 17.4 m s $^{-1}$, corresponding to a maximum *WSV* value of -14.7 m s $^{-1}$. The most severe wind shear occurred at 17:44, registering a remarkable speed difference of 22.4 m s $^{-1}$ within 6.7–14.3 km distance, corresponding to the *WSV* value of -18.7 m s $^{-1}$, which would pose serious risk to aircraft

operations during take-off and landing stages.

Fig. 5 presents the identification results of wind shear and shear lines in the airport area at different times, along with the 3° PPI scanning. For this case, the shear intensity within the shear center is significantly high, while weak wind shear also occurs in the surrounding areas. If the threshold is set too low, it will compromise the accurate identification of

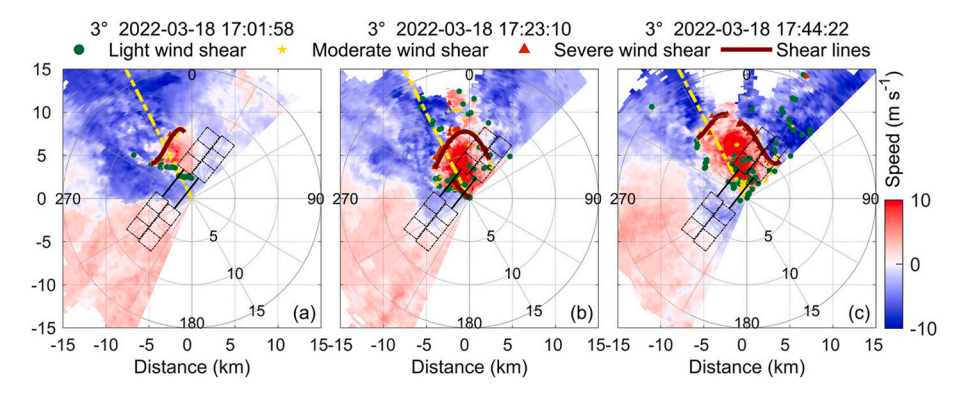


Fig. 5. The results of shear lines identification during convective weather process. (a)-(c) show the identification of wind shear and shear lines and the results of PPI scanning at different times of 3° elevation angle, respectively. The yellow dotted lines are the cross sections corresponding to each radial speed in Fig. 4. Red triangles indicate severe wind shear, characterized by a *WSV* value exceeding 12 m s^{-1} . Green circles represent light wind shear, with a *WSV* value below 8 m s^{-1} , while yellow pentagrams represent moderate wind shear with an intermediate *WSV* value. (For interpretation of the references to colour in this figure legend, the reader is referred to the web version of this article.)

the shear line. Consequently, wind shear points with WSV value exceeding 8 m s⁻¹ were selected for shear line fitting. The PPI scanning results reveal the presence of wind shear near the northern runway, characterized by prevailing northerly winds in the near field and southerly winds in the far. At 17:01, the light and moderate wind shear were detected predominantly in the area. A shear line was identified near north of the left runway, at a distance of 6–8 km from the lidar. At 17:23, the intensity of the wind shear detected in the area increased, and the influence area of shear line expanded, extending over north runway. Notably, the shear line was curved. At 17:44, with the increasing extent of low-level northerly winds and the intensification of convective activity, two shear lines associated with severe wind shear were identified. These conditions would pose a significant threat to aircraft landing and take-off operations near north runway.

Fig. 6 presents radial wind shear identification results at three different times (22:46–23:15) during a gust event on March 14, 2022. Given the PPI revealed comparatively lower wind speeds than those in convective events, the wind shear intensity factor $\Delta V/(\Delta L)^{1/3}$ threshold was reduced to 0.4 for enhanced detection sensitivity. The detection at 22:46 identified moderate wind shear at about 4.1 km from lidar, exhibiting a wind speed difference of 7.5 m s $^{-1}$ and the WSV value of 9.8 m s $^{-1}$. It was observed that wind shear gradually strengthened, with the detection at 23:15 capturing shear activity within the 1.3–10.5 km distance. This shear displayed maximum speed difference of 12.5 m s $^{-1}$ and corresponding maximum WSV value of 10.7 m s $^{-1}$. The gust-induced wind shear intensity is weaker compared to convective weather.

Fig. 7 presents the identification results of wind shear and shear lines in the airport area at different times, along with the 2° PPI scanning. Given the weaker wind shear intensity in gust events relative to convective weather, the classification criteria were adjusted. Distinct markers denote shear points of varying intensities: red triangles represent severe shear ($WSV > 8 \text{ m s}^{-1}$), yellow pentagrams indicate moderate shear ($6-8 \text{ m s}^{-1}$), and green circles mark light shear ($<6 \text{ m s}^{-1}$). PPI scanning results revealed northeasterly winds in the near field transitioning to southwesterly flows aloft over south glide path. The shear line propagated southwestward under northeasterly flows, exhibiting a relatively straight shape contrasting with the curved line observed in the convective weather.

3.2. Shear identification and forecasting of urban surface

China's low-altitude aviation economy has entered a phase of rapid development recently (Huang, 2025), including general aviation for

emergency rescue, urban logistics flight, and manned flight, etc. Wind shear over complex urban underlying surfaces can cause low-speed, small aircraft to lose control or even crash, as small aircraft is sensitive to weak wind shear. There is an urgent need to expand wind shear detection capabilities from airports to urban scenarios to cater for low altitude operations such as electric vertical take-off and landing (eVTOL) aircraft and UAVs (Gultepe, 2023).

In contrast to airport with homogeneous terrain, urban surface is relatively complex. Urban low-altitude wind turbulence poses a significant challenge to accurate wind shear identification. To validate identification ability of the proposed method in complex wind fields, the experiment is conducted at Gulou District, Nanjing city, Jiangsu province $(32^{\circ}02'N, 118^{\circ}43'E)$. Fig. 8a shows the location of the Doppler wind lidar. The lidar is fixed at the top of a building with height of 150 m, and the typical detection range is 15 km. Wind detection results from August 7, 2024, are selected for analysis.

Fig. 9 shows the results of wind shear and shear lines identification and PPI scanning at 0° elevation angle from 17:05 to 18:42. Given the complexity of urban surface, PPI scanning revealed lower wind speed accompanied by diverse weak wind shear within the area. A threshold set too high would fail to detect such shear lines—yet these shear lines could pose a significant impact on low-altitude UAVs operating in urban environments. To effectively identify weak shear, the wind shear intensity factor $\Delta V/(\Delta L)^{1/3}$ threshold was reduced to 0.3, with classification criteria defining light shear as $WSV < 6~{\rm m~s^{-1}}$ and severe shear $> 8~{\rm m~s^{-1}}$.

According to the results shown in Fig. 9, most of the detected wind shear is light. A converging shear line 1 was detected on the southeast side of the region, moving away from the lidar driven by the northwesterly winds. Shear line 2 was initially detected at about 9 km distance and moved towards the southeast direction, which was formed through convergence of northwesterly and southeasterly flows. Due to the low wind speeds behind the line, the shear line 2 moved relatively slowly. At 18:17, shear line 3 manifested at approximately 13 km distance. Northwesterly winds of approximately 10 m s $^{-1}$ behind shear line 3 accelerated its southeastward movement, causing it to merge with shear line 2 then approached the lidar.

The movement of the shear line is highly correlated with the wind field behind it, which serves as the fundamental basis for shear line forecasting. Taking shear line 1 as an example, which was located at about 9.0 km at 17:05. And at 17:17, the shear line had advanced to about 10.0 km. The propagation velocity aligned with the mean wind speed in the approximately 1 km region behind it. Single-step movement

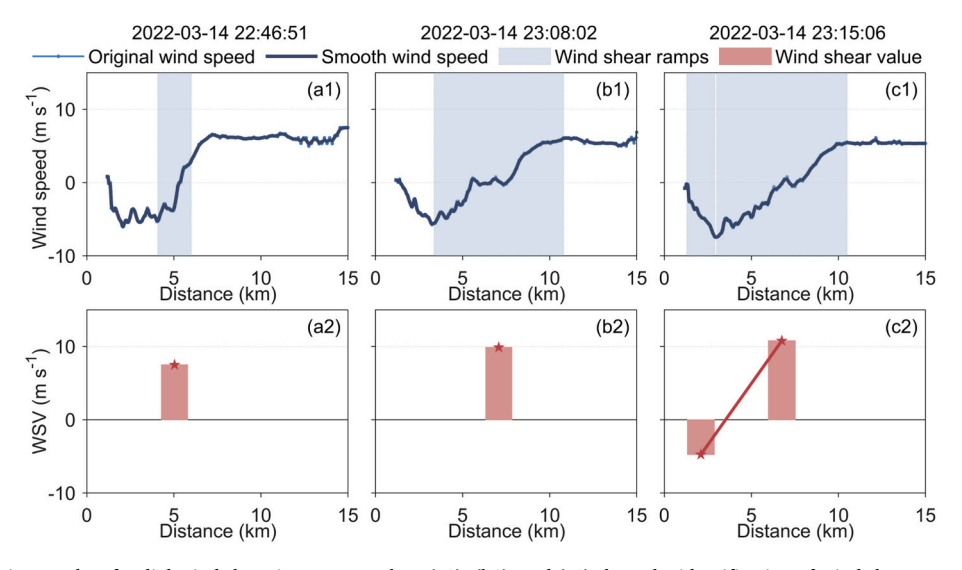


Fig. 6. Typical identification results of radial wind shear in gusty weather. (a1), (b1), and (c1) show the identification of wind shear ramps at different times for 2° elevation angle and 215° azimuthal angle, respectively. (a2), (b2), and (c2) represent the *WSV* value of each wind shear ramp.

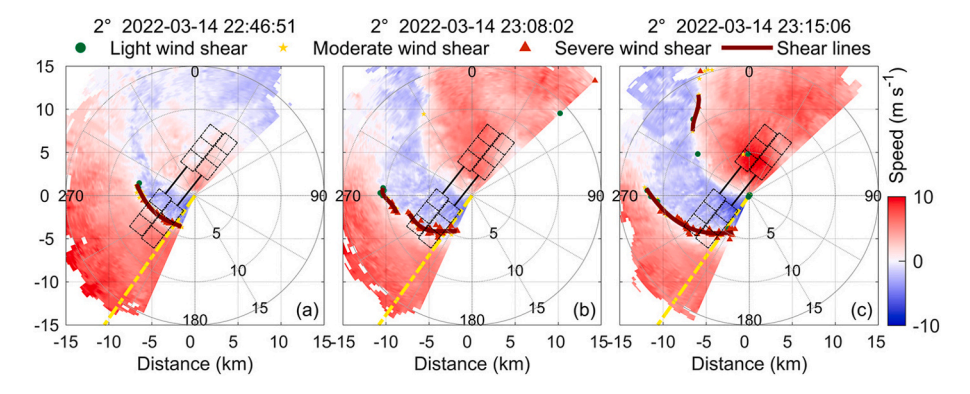


Fig. 7. The results of shear lines identification during gusty weather process. (a)-(c) show the identification of wind shear and shear lines and the results of PPI scanning at different times of 2° elevation angle, respectively. The yellow dotted lines are the cross sections corresponding to each radial speed in Fig. 6. Red triangles indicate severe wind shear, characterized by a WSV value exceeding 8 m s⁻¹. Green circles represent light wind shear, with a WSV value below 6 m s⁻¹, while yellow pentagrams represent moderate wind shear with an intermediate WSV value. (For interpretation of the references to colour in this figure legend, the reader is referred to the web version of this article.)

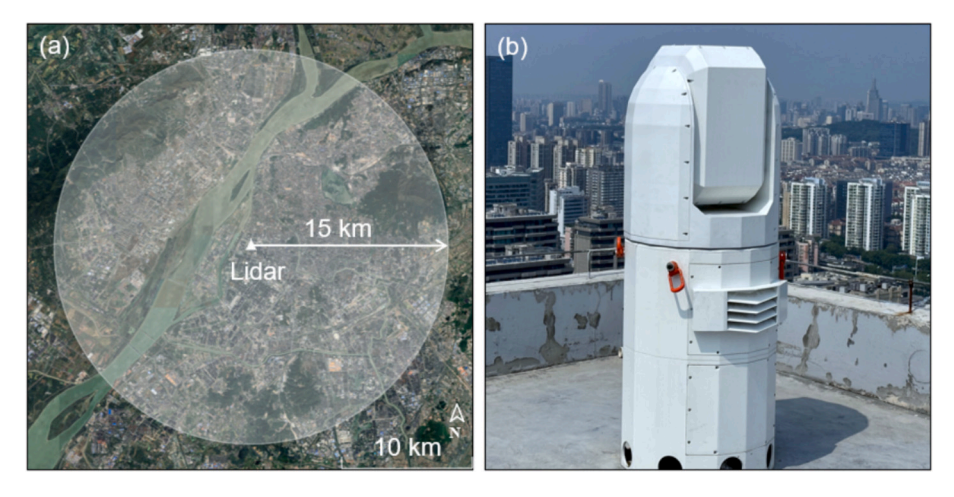


Fig. 8. Lidar station location and picture. (a) shows the lidar position of Gulou District, Nanjing. (b) is a photo of the lidar.

forecasting for shear lines 1–3 was conducted by the analysis of wind field near the shear lines, combined with lidar-detected arrival time. Specifically, calculate the mean wind speed in about 1 km area behind the shear line as its propagation speed; Then estimate the arrival time at the next position using this speed; Finally compare the forecasted time with actual lidar-detected time to assess accuracy.

The forecasting results along with error analysis results are presented in Fig. 10. Fig. 10a illustrates the movement forecasting of shear line 1. The forecasting revealed that shear line 1 reached about 12.0 km at 17:40, while the lidar-detected time was 17:41, only with a 1-min time error. Subsequent moved to about 14.0 km at 17:54, with forecasting error of 1 min. At 17:59, the shear line reached about 15.0 km, with forecasting time versus lidar- detected diverging by 6 min. Fig. 10b illustrates the movement forecasting of shear line 2, which was located at about 9.0 km at 18:05 then gradually approaching lidar. Fig. 10c illustrates that shear line 3 initially occurred at about 13.0 km. The forecasting revealed the shear lines 2 and 3 merged together at 18:30. Subsequently the lidar showed them at 2.0 km at 18:42, with forecasting time errors within 3 min. During this process, the longest forecasting time is 25 min.

4. Discussion and conclusion

This study develops a real-time wind shear and shear line detection method using Doppler wind lidar, integrating ramp detecting algorithm with the dual filtering mechanism and shear point clustering. The method uses PPI scanning to effectively achieve the expansion of the detection area from glide path areas to the full region. Gradually expanding the length of wind shear ramp can effectively avoid missing identification. The dual filtering mechanism effectively eliminates two interference types: short-range high-gradient shear and long-range weak shear gradients. Compared to previous algorithms, the method enables selective identification of diverse wind shear to suit different scenarios through dynamic threshold adjustment. In addition, the shear lines can be derived solely by real-time detection of lidar.

Experimental results demonstrate successful identification of gust front-induced and convective shear lines in airport, along with effective forecasting of urban shear lines under complex surface. It shows that there are differences in the distribution of shear lines under different weather conditions. Compared with gusty weather, the shear lines generated by strong convective weather are more curved and stronger. When convection develops more vigorously, the more curved the shear lines are. Due to the complexity of the urban surface, the distribution of wind shear is chaotic and the intensity is weak. Accurate identification of shear line features contributes to the study of weather change processes. In addition, experiments revealed a strong correlation between shear line movement and its post-shear wind field. A maximum forecast of approximately 25 min for urban low-altitude shear lines was successfully achieved. This not only facilitates a deeper understanding and tracking of the atmospheric processes associated with shear lines but also effectively mitigates flight risks from abrupt weather changes, thereby supporting low-altitude operational safety.

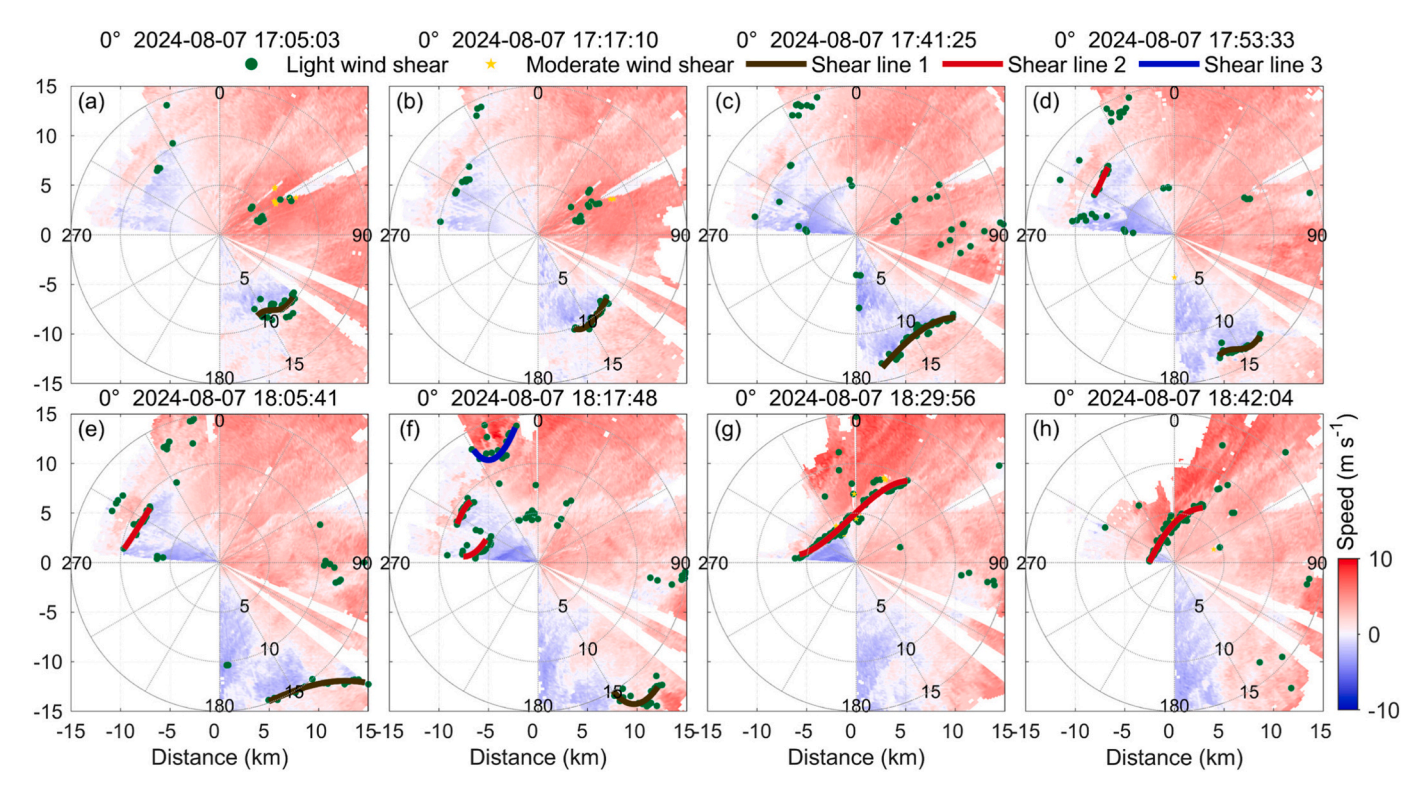


Fig. 9. Results of wind shear and shear lines identification and 0° PPI scanning. (a)-(h) are the identification results of shear lines from 17:05 to 18:42 on August 7, 2024. Red triangles indicate severe wind shear, characterized by a *WSV* value exceeding 8 m s⁻¹. Green circles represent light wind shear, with a *WSV* value below 6 m s⁻¹, while yellow pentagrams represent moderate wind shear with an intermediate *WSV* value. (For interpretation of the references to colour in this figure legend, the reader is referred to the web version of this article.)

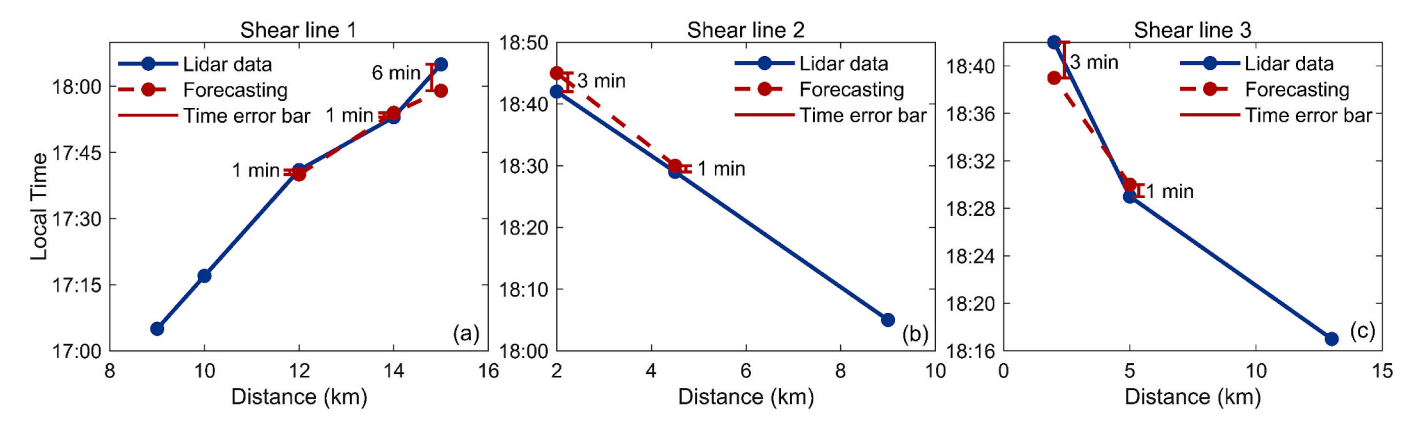


Fig. 10. Lidar detections and forecasting results. (a)-(c) show forecasting results along with time errors of shear lines 1, 2 and 3, respectively. The red dots demonstrate the forecasting time, while the blue dots indicate the lidar-detected arrival time of the shear lines. (For interpretation of the references to colour in this figure legend, the reader is referred to the web version of this article.)

However, there are still some issues that deserve consideration in the future work. Although the proposed method has been well implemented for the three typical scenarios with dynamic threshold, additional cases are still required to optimize the strategy for threshold selection. An adaptive threshold model that autonomously adjusts to real-time wind field characteristics can be developed to reduce manual intervention. Additionally, the method relies on lidar data, which may be impacted by saturated weather (e.g., thunderstorms, heavy rain), beam blockages in complex terrains (Yang et al., 2024), and limited detection range (Gultepe et al., 2018). Future advancements will enhance lidar hardware parameters and supplement with multi-sensor fusion to improve identification quality.

CRediT authorship contribution statement

Anning Chen: Writing – review & editing, Writing – original draft, Visualization, Supervision, Software, Methodology, Formal analysis, Data curation. Jinlong Yuan: Methodology, Conceptualization. Haoyu Yang: Writing – review & editing, Formal analysis. Jiaxiu Liu: Writing – review & editing, Formal analysis. Yuanhao Gu: Writing – review & editing, Formal analysis. Tianwen Wei: Writing – review & editing, Formal analysis. Haiyun Xia: Writing – review & editing, Formal analysis.

Financial support

This study has been supported by the Natural Science Foundation of

Jiangsu Province (BK20230434), National Natural Science Foundation of China (42405137), and Aeronautical Science Foundation of China (202300220R2001).

Declaration of competing interest

The authors declare that they have no known competing financial interests or personal relationships that could have appeared to influence the work reported in this paper.

Data availability

Measurement data from the field campaign used in this study are available from the corresponding author upon request (yuaniinlong@nuist.edu.cn).

References

- Baranov, N., Lemishchenko, E., 2020. Integrated algorithm of the wind shear calculating from lidar data. In: International Conference of Numerical Analysis and Applied Mathematics Icnaam, 2019, pp. 420068-1–420068-4. https://doi.org/10.1063/ 5.0026963.
- Biard, J.C., Kunkel, K.E., 2019. Automated detection of weather fronts using a deep learning neural network. Adv. Stat. Clim. Meteorol. Oceanogr. 5, 147–160. https://doi.org/10.5194/ascmo-5-147-2019.
- Bluestein, H.B., Speheger, D.A., 1995. The dynamics of an upper-level trough in the baroclinic westerlies: analysis based upon data from a wind profiler network. Mon. Weather Rev. 123, 2369-2383. https://doi.org/10.1175/1520-0493(1995) 123-2369:TDOAUL-2.0.CO:2.
- Cai, Y., Li, Q., Fan, Y., Zhang, L., Huang, H., Ding, X., 2021. An automatic trough line identification method based on improved UNet. Atmos. Res. 264, 105839–105852. https://doi.org/10.1016/j.atmosres.2021.105839.
- Chan, P.W., 2012. Application of LIDAR-based F-factor in windshear alerting. Meteorol. Z. 21, 193–204. https://doi.org/10.1127/0941-2948/2012/0321.
- Chan, P.W., Shun, C.M., 2008. Applications of an infrared Doppler Lidar in Detection of Wind Shear. J. Atmos. Ocean. Technol. 25, 637–655. https://doi.org/10.1175/ 2007JTECHA1057.1.
- Chan, P.W., Hon, K.K., Shin, D.K., 2011. Combined use of headwind ramps and gradients based on LIDAR data in the alerting of low-level windshear/turbulence. Meteorol. Z. 20, 661–670. https://doi.org/10.1127/0941-2948/2011/0242.
- Gultepe, I., 2023. A review on weather impact on aviation operations: visibility, wind, precipitation, icing. J. Airline Oper. Aviat. Manag. 2, 1–44. https://doi.org/10.56801/jaoam.v2i1.1.
- Gultepe, I., Agelin-Chaab, M., Komar, J., Elfstrom, G., Boudala, F., Zhou, B., 2018.
 A meteorological supersite for aviation and cold weather applications. Pure Appl. Geophys. 176, 1977–2015. https://doi.org/10.1007/s00024-018-1880-3.
- Hermes, L.G., Witt, A., Smith, S.D., Klingle-Wilson, D., Morris, D., Stumpf, G.J., Eilts, M. D., 1993. The gust-front detection and wind-shift algorithms for the terminal Doppler weather radar system. J. Atmos. Ocean. Technol. 10, 693–709. https://doi.org/10.1175/1520-0426(1993)010<0693:TGFDAW>2.0.CO;2.
- Hon, K.K., Chan, P.W., 2014. Application of LIDAR-derived eddy dissipation rate profiles in low-level wind shear and turbulence alerts at Hong Kong International Airport. Meteorol. Appl. 21, 74–85. https://doi.org/10.1002/met.1430.
- Huang, X., 2025. The small-drone revolution is coming scientists need to ensure it will be safe. Nature 637, 29–30. https://doi.org/10.1038/d41586-024-04167-7.
- Huang, Y., Meng, Z., Li, W., Bai, L., Meng, X., 2019. General features of radar-observed boundary layer convergence lines and their associated convection over a sharp vegetation-contrast area. Geophys. Res. Lett. 46, 2865–2873. https://doi.org/ 10.1029/2018gl081714.
- Huang, X., Zheng, J., Shao, A., Xu, D., Tian, W., Li, J., 2024. Study of low-level wind shear at a Qinghai-Tibetan Plateau Airport. Atmos. Res. 311, 107680. https://doi. org/10.1016/j.atmosres.2024.107680.
- ICAO, 2005. Manual on Low-Level Wind Shear. International Civil Aviation Organization Montréal, QC, Canada.
- Lagerquist, R., McGovern, A., Gagne II, D.J., 2019. Deep learning for spatially explicit prediction of synoptic-scale fronts. Wea. Forecasting. 34, 1137–1160. https://doi. org/10.1175/WAF-D-18-0183.1.

- Lee, Y., Chan, P.W., 2013. LIDAR-based F-factor for wind shear alerting: different smoothing algorithms and application to departing flights. Meteorol. Appl. 21, 86–93. https://doi.org/10.1002/met.1434.
- Liu, Z., Barlow, J.F., Chan, P.W., Fung, J.C.H., Li, Y., Ren, C., Mak, H.W.L., Ng, E., 2019. A review of progress and applications of pulsed Doppler wind LiDARs. Remote Sens 11, 2522–2568. https://doi.org/10.3390/rs11212522.
- Liu, J., Chen, H., Xu, J., 2022. Climatology of shear line and related rainstorm over the Southern Yangtze River Valley based on an improved intelligent identification method. J. Trop. Meteorol. 28, 413–424. https://doi.org/10.46267/j.1006-8775.2022.031.
- Luers, J., Hairies, P., 1983. Heavy rain influence on airplane accidents. J. Aircr. 20, 187–191. https://doi.org/10.2514/3.44850.
- Luo, Z., Song, X., Yin, J., Bu, Z., Chen, Y., Yu, Y., Zhang, Z., 2024. Comparison and verification of coherent Doppler Wind Lidar and radiosonde data in the Beijing Urban Area. Adv. Atmos. Sci. 41, 2203–2214. https://doi.org/10.1007/s00376-024 3240-9
- Nechaj, P., Gaál, L., Bartok, J., Vorobyeva, O., Gera, M., Kelemen, M., Polishchuk, V., 2019. Monitoring of low-level wind shear by ground-based 3D Lidar for increased flight safety, protection of human lives and health. Int. J. Environ. Res. Public Health 16, 4584–4609. https://doi.org/10.3390/ijerph16224584.
- Piva, E.D., Gan, M.A., Rao, V.B., 2008. An objective study of 500-hPa moving troughs in the Southern Hemisphere. Mon. Weather Rev. 136, 2186–2200. https://doi.org/ 10.1175/2007mwr2135.1.
- Su, L., Lu, C., Yuan, J., Wang, X., He, Q., Xia, H., 2024. Measurement report: the promotion of the low-level jet and thermal effects on the development of the deep convective boundary layer at the southern edge of the Taklimakan Desert. Atmos. Chem. Phys. 24, 10947–10963. https://doi.org/10.5194/acp-24-10947-2024.
- Thobois, L., Cariou, J.P., Gultepe, I., Geophysics, A., 2018. Review of lidar-based applications for aviation weather. Pure Appl. Geophys. 176, 1959–1976. https://doi.org/10.1007/s00024-018-2058-8.
- Tian, H., Hu, Z., Wang, F., Xie, P., Xu, F., Leng, L., 2024. Radar echo recognition of gust front based on deep learning. Remote Sens 16, 439–451. https://doi.org/10.3390/ rs16030439
- Wadler, J.B., Cione, J.J., Rogers, R.F., Fischer, M.S., 2023. On the distribution of convective and stratiform precipitation in tropical cyclones from Airborne Doppler Radar and its relationship to intensity change and environmental wind shear direction. Mon. Weather Rev. 151, 3209–3233. https://doi.org/10.1175/mwr-d-23-0048.1.
- Wang, L., Qiang, W., Xia, H., Wei, T., Yuan, J., Jiang, P., 2021. Robust solution for boundary layer height detections with coherent Doppler Wind Lidar. Adv. Atmos. Sci. 38, 1920–1928. https://doi.org/10.1007/s00376-021-1068-0.
- Wang, M., Wei, T., Lolli, S., Wu, K., Wang, Y., Hu, H., Yuan, J., Tang, D., Xia, H., 2024. A long-term Doppler wind LiDAR study of heavy pollution episodes in western Yangtze River Delta region, China. Atmos. Res. 310. https://doi.org/10.1016/j. atmosres.2024.107616.
- Wilson, J.W., Roberts, R.D., Kessinger, C., McCarthy, J., 1984. Microburst wind structure and evaluation of Doppler radar for Airport wind shear detection. J. Appl. Meteorol. Climatol. 23, 898–915. https://doi.org/10.1175/1520-0450(1984)023<0898: MWSAEO>2.0.CO:2.
- Woodfield, A.A., Woods, J.F., 1983. Worldwide experience of wind shear during 1981-1982. In: Royal Aircraft Establishment: Bedford, UK.
- Xia, H., Chen, Y., Yuan, J., Su, L., Yuan, Z., Huang, S., Zhao, D., 2024. Windshear detection in rain using a 30 km Radius Coherent Doppler Wind Lidar at mega Airport in Plateau. Remote Sens 16, 924–936. https://doi.org/10.3390/rs16050924.
- Yang, H., Yuan, J., Guan, L., Su, L., Wei, T., Xia, H., 2024. Reconstruction for beam blockage of lidar based on generative adversarial networks. Opt. Express 32, 14420–14434. https://doi.org/10.1364/OE.520528.
- Yuan, J., Su, L., Xia, H., Li, Y., Zhang, M., Zhen, G., Li, J., 2022. Microburst, windshear, gust front, and vortex detection in mega Airport using a single coherent Doppler Wind Lidar. Remote Sens 14, 1626–1639. https://doi.org/10.3390/rs14071626.
- Zhang, H., Wu, S., Wang, Q., Liu, B., Yin, B., Zhai, X., Technology, 2019. Airport low-level wind shear lidar observation at Beijing Capital International Airport. Infrared Phys. Technol. 96, 113–122. https://doi.org/10.1016/j.infrared.2018.07.033.
- Zhao, S., Shan, Y., 2022. Study of the algorithm for wind shear detection with Lidar based on shear intensity factor. Algorithms 15, 133–147. https://doi.org/10.3390/ a15040133.
- Zhao, S., Yang, C., Shan, Y., Zhu, F., 2025. Identification and analysis of wind shear within the transiting frontal system at Xining International Airport using Lidar. Remote Sens 17, 732–755. https://doi.org/10.3390/rs17050732.